Influence of satellite-derived photolysis rates and NO_x emissions on Texas ozone modeling

Wei Tang[1,*], Daniel S. Cohan[1], Arastoo Pour-Biazar[2], Lok N. Lamsal[3,4], Andrew T. White[5], Xue Xiao[1], Wei Zhou[1], Barron H. Henderson[6], Benjamin F. Lash[1]

[1]*Department of Civil and Environmental Engineering, Rice University, 6100 Main Street MS 519, Houston, TX 77005, USA; Email: cohan@rice.edu*

[2]*Earth System Science Center, University of Alabama, Huntsville, AL, USA*

[3]*NASA Goddard Space Flight Center, Greenbelt, MD, USA*

[4]*Goddard Earth Sciences Technology & Research, Universities Space Research Association, Columbia, MD, USA*

[5]*Department of Atmospheric Science, University of Alabama, Huntsville, AL, USA*

[6]*Department of Environmental Engineering Sciences, University of Florida, Gainesville, FL, USA*

[*]*now at: Chinese Research Academy of Environmental Sciences, Beijing, China*

Abstract

Uncertain photolysis rates and emission inventory impair the accuracy of state-level ozone (O_3) regulatory modeling. Past studies have separately used satellite-observed clouds to correct the model-predicted photolysis rates, or satellite-constrained top-down NO_x emissions to identify and reduce uncertainties in bottom-up NO_x emissions. However, the joint application of multiple satellite-derived model inputs to improve O_3 State Implementation Plan (SIP) modeling has rarely been explored. In this study, Geostationary Operational Environmental Satellite (GOES) observations of clouds are applied to derive the photolysis rates, replacing those used in Texas SIP modeling. This changes modeled O_3 concentrations by up to 80ppb and improves O_3 simulations by reducing modeled normalized mean bias (NMB) and normalized mean error (NME) by up to 0.1. A sector-based discrete Kalman filter (DKF) inversion approach is incorporated with the Comprehensive Air Quality Model with extensions (CAMx)-Decoupled

Direct Method (DDM) model to adjust Texas NO_x emissions using a high resolution Ozone Monitoring Instrument (OMI) NO_2 product. The discrepancy between OMI and CAMx NO_2 vertical column densities (VCDs) is further reduced by increasing modeled NO_x lifetime and adding an artificial amount of NO_2 in the upper troposphere. The region-based DKF inversion suggests increasing NO_x emissions by 10-50% in most regions, deteriorating the model performance in predicting ground NO_2 and O_3, while the sector-based DKF inversion tends to scale down area and non-road NO_x emissions by 50%, leading to a 2-5ppb decrease in ground 8-h O_3 predictions. Model performance in simulating ground NO_2 and O_3 are improved using sector-based inversion constrained NO_x emissions, with 0.25 and 0.04 reductions in NMBs and 0.13 and 0.04 reductions in NMEs, respectively. Using both GOES-derived photolysis rates and OMI-constrained NO_x emissions together reduces modeled NMB and NME by 0.05 and increases the model correlation with ground measurement in O_3 simulations and makes O_3 more sensitive to NO_x emissions in the O_3 non-attainment areas.

1. Introduction

Tropospheric O_3 is a secondary air pollutant formed via the reactions between nitrogen oxides ($NO_x = NO + NO_2$) and volatile organic compounds (VOCs) with heat and sunlight (Seinfeld and Pandis, 2006). Eastern Texas is one of the most populous areas in the United States and has been suffering from O_3 pollution for decades due to large anthropogenic emission sources such as motor vehicles, petrochemical facilities, and coal-burning power plants with unique meteorological conditions of extended heat and humidity and intense solar radiation (Kleinman et al., 2002; Ryerson et al., 2003; Daum et al., 2004; Rappenglück et al., 2008; Kim et al., 2011; Zhou et al., 2014).

In eastern Texas, several regions require careful air quality planning for O_3 reductions. First and foremost, the Houston-Galveston-Brazoria (HGB) region and the Dallas-Fort Worth (DFW) region exceed the 2008 O_3 National Ambient Air Quality Standard (NAAQS) of 75 ppb and thus are both classified by US Environmental Protection Agency (US EPA) as O_3 non-attainment areas. Next, Beaumont-Port Arthur (BPA), Northeast Texas (NE Texas), and Austin and San Antonio regions require attention for closely approaching that standard (Gonzales and Williamson, 2011).

To comply with the O_3 NAAQS, the U.S. EPA requires the Texas Commission on Environmental Quality (TCEQ) to identify regulatory strategies using photochemical air quality models for attaining the O_3 standard in non-attainment areas. However, model uncertainties may impair the accuracy of model performance and potentially misdirect emission control strategies (Fine et al., 2003; Digar and Cohan, 2010; Simon et al., 2012). Recent studies show that uncertain bottom-up emission inventories and modeled photolysis rates are two leading uncertainties in O_3 modeling (Deguilaume et al., 2007; Digar et al., 2011) and can significantly impact simulated O_3 concentrations and their sensitivities in Texas (Cohan et al., 2010; Xiao et al., 2010). Hence, identifying and reducing these uncertainties are essential to ensuring the reliability of regulatory decision making.

Direct measurements of emissions and photolysis rates are spatially limited and impractical to perform covering the entire modeling domain. However, satellite-based measurements provide a valuable opportunity to observe some atmospheric parameters and air pollutants from space and generate a rich measurement dataset with great spatial coverage. Pour-Biazar et al. (2007) used the GOES-based cloud information to reproduce photolysis rates in the

Community Multiscale Air Quality (CMAQ) model. Results showed large differences between model-predicted and satellite-derived photolysis rates, leading to significant changes in modeled O_3 concentrations. Guenther et al. (2012) found that the Weather Research and Forecasting (WRF) and MM5 models, which are usually used to generate meteorological fields for CAMx or CMAQ, underpredict cloud fractions, leading to more modeled solar radiation reaching the ground and overestimations of modeled photolysis rates and sunlight-sensitive biogenic emissions.

Studies using satellite NO_2 measurements to create top-down NO_x emissions for atmospheric modeling have also shown promising results (Streets et al., 2013; Martin et al., 2003; Müller and Stavrakou, 2005; Jaeglé et al., 2005; Lin et al., 2010; Konovalov et al., 2006, 2008; Napelenok et al., 2008; Kurokawa et al., 2009; Zhao and Wang, 2009; Chai et al., 2009; Zyrichidou et al., 2015). Most recently, Tang et al. (2013) performed region-based DKF inversions using OMI NO_2 data to adjust NO_x emission inventory used in Texas SIP modeling; however, results showed that the region-based DKF inversions with National Aeronautics and Space Administration (NASA) OMI NO_2 standard product, version 2, tended to scale up the NO_x emission inventory by factors of 1.02 to 1.84 and deteriorated model performance as evaluated by ground NO_2 and O_3 monitors.

A challenge of using satellite data for inverse modeling is that atmospheric models are primarily evaluated based on ground-level data, and may not accurately simulate pollutants aloft. Several studies (Hudman et al., 2007; Henderson et al., 2011; Allen et al., 2012; ENVIRON, 2013) have demonstrated that models tend to underestimate upper tropospheric NO_2 level even after lightning and aviation NO_x sources are included. Though the reason is unclear, underestimation could result from errors in the chemical mechanism in simulating NO_x sinks (Mollner et al., 2010; Henderson et al., 2012, Lin et al., 2012, Stavrakou et al., 2013). Efforts to eliminate low bias for upper tropospheric NO_2 simulations over Texas have been unsuccessful to date (ENVIRON 2013). Another discrepancy often noted between models and satellite data is a narrower spread between urban and rural NO_2 in satellite observations (Streets et al., 2013). Recently developed high resolution OMI NO_2 retrievals increase the rural-urban spread, which may decrease the difference between models and satellite observations.

In this work, first, GOES-derived photolysis rates are applied to the CAMx model, and the influence on the modeled NO_2 and O_3 is investigated. Second, the model shortcomings of underestimating upper tropospheric and rural NO_2 demonstrated in Tang et al. (2013) are further addressed by comparing with aircraft measurements and reducing the reaction rate constant of the reaction OH + NO_2 to increase modeled NO_x lifetime. Third, the sector-based DKF inversion using the recently developed NASA high resolution OMI NO_2 product to Texas NO_x emissions is explored and compared to the region-based DKF inversion. In addition, inverse modeling is extended to adjust Texas VOC emissions via directly comparing modeled VOC concentrations with ground observations (Supplement, Sect. 4).

2. Methodology

2.1 CAMx modeling

CAMx version 5.3 (ENVIRON, 2010) with the Carbon Bond version 2005 (CB-05) chemical mechanism was used to simulate a SIP modeling episode developed by TCEQ for the HGB O_3 attainment demonstration (Fig. 1) from 13 August to 15 September 2006, coinciding with the intensive measurement campaign TexAQS 2006. The meteorology fields were modeled by the

NCAR/Penn State (National Center for Atmospheric Research/Pennsylvania State University) Mesoscale Model, Version 5, release 3.7.3 (MM5v.3.7.3) (Grell et al., 1994), and the boundary conditions were taken from the Model for Ozone and Related Chemical Tracers (MOZART) global model (ENVIRON, 2008). The base case emission inventory for HGB SIP modeling was provided by TCEQ (TCEQ, 2010). Lightning and aviation NO_x emissions were added into the base emission inventory. The lightning NO_x emission is developed based on the measured National Lightning Detection Network (NLDN) data with intra-cloud flashes assumed to be three times of cloud-to-ground flashes and 500 moles NO emissions per flash (Kaynak et al., 2008), and the aviation NO_x emissions, obtained from the Emission Database for Global Atmospheric Research (EDGAR), were placed at the model height of 9km. The soil NO_x emission was doubled from its base value because the Yienger and Levy method (YL95) (Yienger and Levy, 1995) has been found to underpredict soil NO_x by around a factor of 2 over the United States (Hudman et al., 2010). More details about the model inputs and configurations, the emission inventory development, and evaluations of model meteorological inputs can be found in Tang et al. (2013).

2.2 GOES-derived photolysis rates

The photolysis rate calculations in CAMx include two steps (ENVIRON, 2010). First, a Tropospheric Ultraviolet and Visible (TUV) Radiation Model developed by the National Center for Atmospheric Research (NCAR) is used to generate a multi-dimensional table of clear sky photolysis rates (Madronich, 1987; NCAR, 2014) as inputs for the CAMx model as shown in Eq. (1).

Clear sky photolysis rates (s^{-1}) are calculated as:

$$J = \int_{\lambda_1}^{\lambda_2} \sigma(\lambda)\varphi(\lambda)F(\lambda)d\lambda \qquad (1)$$

where $\sigma(\lambda)$ ($m^2/molecule$) is the absorption cross-section, λ is the wavelength (μm), $\varphi(\lambda)$ is the quantum yield (*molecules/photon*), and $F(\lambda)$ is the actinic flux ($photons/m^2/s/\mu m$).

Second, the tabular clear sky photolysis rates are interpolated into each grid cell in the modeling domain and adjusted based on cloud information generated by the meteorology model in standard operational procedure, as shown in Eqs. (2) and (3). Below the cloud, photolysis rates are adjusted as (Chang et al., 1987):

$$J_{below} = J_{clear}\left[1 + f_c(1.6\ tr_c \cos(\theta) - 1)\right] \qquad (2)$$

Above the cloud, photolysis rates are modified as:

$$J_{above} = J_{clear}\left[1 + f_c \cos(\theta)(1 - tr_c)\right] \qquad (3)$$

where f_c is the cloud fraction for a grid cell, tr_c is cloud transmissivity at each model grid layer, and θ is the solar zenith angle.

In CAMx, tr_c is calculated using Eq. (4) (Stephens, 1978),

$$tr_c = \frac{5 - e^{-\tau_c}}{4 + 3\tau_c(1-\beta)} \qquad (4)$$

where τ_c is the cloud optical depth simulated in the model and β is the scattering phase-function asymmetry factor assumed to be 0.86 (Chang et al., 1987). The f_c in each grid cell is predicted by the MM5 model.

GOES-observed cloud properties recover f_c and broadband tr_c, which can be used directly in Eqs. (2) and (3) to adjust photolysis rates below and above the clouds, bypassing the need for estimating those values in the model. Within the cloud, the photolysis rates are adjusted via the interpolation of calculated values between satellite-retrieved cloud top and model-estimated cloud base. GOES is capable of measuring cloud properties with spatial resolution down to 1-km and temporal resolution down to an hour or less (Haines et al., 2004), ensuring the sufficient spatial and temporal data coverage for the modeling episode. In this study, hourly GOES observations with integrated 12km cloud properties from sub-pixels have been used. However, due to the satellite data availability, satellite-retrieved f_c and broadband tr_c may not be available in the early morning and late afternoon. In such cases, the f_c and tr_c generated by standard operational procedures in CAMx will be used. More details regarding satellite retrievals of f_c and tr_c can be found at Pour-Biazar, et al. 2007.

2.3 Emission regions and sectors for the inversion

As in Tang et al. (2013), an inversion region inside the 12km model domain is designed for both region-based and sector-based DKF inversions, including five urban areas HGB, DFW, BPA, NE Texas, and Austin and San Antonio, surrounded by a north rural area (N rural) and a south rural area (S rural) (Fig. 1).

Six separate NO_x emission sectors, area, non-road mobile, on-road mobile, biogenic, electric generating units (EGU) and non-EGU point sources are provided by TCEQ. Lightning and aviation NO_x emission sectors were developed in Tang et al. (2013) and added into base emission inventory as independent elevated sources (Table 1). Area sources, including small-scale industry and residential sources such as oil and gas production, gas stations and restaurants, contribute 10% of total emissions in the entire inversion region and 25% in NE Texas in the base inventory. Non-road sources, including construction equipment, locomotives and commercial marine, contribute 14% overall. Mobile source emissions by on-road vehicles contribute 27% of total NO_x emissions and dominate in the cities such as HGB and DFW. The biogenic NO_x source is from soil emissions, which contribute 16% of total NO_x emissions but dominate in remote regions. Lightning and aviation sources contribute 8% and 6% to the total emission, respectively. Non-EGU point sources such as refineries, big boilers and flares, contribute 40% of NO_x emissions in BPA and 21% in HGB, the two regions with most of the petrochemical industries. EGU point emissions are from major power plants with the hourly NO_x emissions measured by continuous emissions monitoring (CEM) systems, which are considered the most accurate NO_x emission source in the bottom-up emission inventory. Thus, in this study, EGU NO_x emissions are assumed to be correct and are not adjusted by DKF inversions.

NO_2 sensitivities to NO_x emission in each emission sector used in the following sector-based DKF inversions are calculated through DDM (Fig. 5). The biogenic, lightning, and non-EGU point sources have their own spatial patterns that differ from the other emission sectors. For example, the aviation source shows strong sensitivity centered from the DFW and HGB regions and slowly spreading elsewhere. The sensitivities from the area, non-road and on-road sources have similar spatial patterns concentrated in urban areas due to strong anthropogenic activities, while the on-road source can be distinguished by the strong highway emissions. Previous studies (Rodgers, 2000; Curci et al., 2010) indicated that the inversion results would be ill-conditioned to estimate strongly overlapped sources. Therefore, in this study, the area and non-road sources are grouped as a single sector in the DKF inversions.

2.4 DKF Inversion

Two DKF inversion approaches, region-based and sector-based, are applied in this study to create top-down NO_x emissions for Texas. The procedure of incorporating DKF method into the CAMx-DDM model was described in detail in Tang et al. (2013).

The DKF inversion process (Prinn 2000), driven by the difference between the measured NO_2 ($\mathbf{C}_{NO_2}^{observed}$) and the modeled NO_2 ($\mathbf{C}_{NO_2}^{predicted}$), seeks the optimal emission perturbation factors ($\hat{\mathbf{x}}$) (a posteriori) by adjusting NO_x emissions in each designated emission region or sector iteratively until each a priori emission perturbation factor ($\mathbf{x}^{-}$) converges within a prescribed criterion, 0.01.

$$\hat{\mathbf{x}}_{\mathrm{NO_x}} = \mathbf{x}^{-}_{\mathrm{NO_x}} + \mathbf{P}^{-}_{\mathrm{NO_x}}\mathbf{S}^{\mathbf{T}}(\mathbf{S}\ \mathbf{P}^{-}_{\mathrm{NO_x}}\mathbf{S}^{\mathbf{T}} + \mathbf{R}_{\mathrm{OMI}})^{\mathbf{-1}}(\mathbf{C}^{\mathrm{observed}}_{\mathrm{NO_2}} - \mathbf{C}^{\mathrm{predicted}}_{\mathrm{NO_2}} - \mathbf{S}\ \mathbf{x}^{-}_{\mathrm{NO_x}}) \tag{5}$$

S in Eq. (5), calculated via DDM in this study, is the first-order semi-normalized sensitivity matrix of NO_2 concentrations to either region-based or sector-based NO_x emissions. The uncertainty value in the measurement error covariance matrix (**R**) for the OMI observed NO_2 is set to 30% (Bucsela et al., 2013) for all diagonal elements. The uncertainties adopted from Hanna et al. (2001) provide the values for each of the diagonal elements in the emission error covariance matrix (**P**). A value of 100% is assigned to each emission region, and to the area, non-road, aviation, on-road, and biogenic emission sectors, but a value of 50% is assigned to the non-EGU point emission sector. The uncertainty of lightning NO_x emissions was estimated in recent studies, ranging from 30% (Martin et al., 2007) to 60% (Schumann and Huntrieser, 2007) on a global scale; thus, the uncertainty value in the lightning sector is set to 50% here. The off-diagonal elements in **P** are set to zero since each emission component is assumed to be independent.

2.5 NO_2 observations

2.5.1 Satellite NO_2 observations

The Dutch-Finnish OMI aboard the NASA Aura satellite measures daily NO_2 at around 13:40 local time (LT) with the highest spatial resolution of 13×24 km^2 at nadir viewpoint (Levelt et al., 2006a, b; Boersma et al., 2007). Tang et al. (2013) used the NASA OMI standard, version 2.1 (Bucsela et al., 2013; Lamsal et al., 2014) NO_2 retrieval with an a priori profile generated from the Global Modeling Initiative (GMI) model to conduct inverse modeling, and reported an overestimation of NO_2 levels in rural areas. More recently, a high resolution OMI NO_2 retrieval was developed based on the NASA standard product, version 2.1, but using an a priori NO_2 profile generated from nested GEOS-Chem simulations ($0.5°\times0.666°$) with a 2005 emission inventory. Because the emission inventory used in GEOS-Chem simulations includes lightning and other elevated sources, it may better represent the upper tropospheric NO_2 in the retrieval; hence, in this study, the high resolution NASA retrieval is chosen for the DKF inversions. In the high resolution NASA product, only the OMI pixels with sizes less than $16\times40km^2$ (scan position 10-50) in the clear-sky condition (cloud radiance fraction < 0.5) are selected in creating the gridded data at $0.1°\times0.1°$ resolution and then mapped to the 12km CAMx modeling domain. Since applying OMI averaging kernels (Eskes and Boersma, 2003) may introduce more uncertainties to the CAMx-derived NO_2 VCDs in this case (Supplement, Sect. 1), the CAMx modeled NO_2 are compared to the OMI NO_2 directly (Supplement, Sect. 1).

2.5.2 Ground and P-3 aircraft NO_2 observations

The CAMx simulated NO_2 is evaluated by both ground and aircraft measurements. The ground-level NO_2 measurements data are taken from the U.S. EPA Air Quality System (AQS) NO_2 ground monitoring network (Fig. 1) (http://www.epa.gov/ttn/airs/airsaqs/). The correction factors (Lamsal et al., 2008; Tang et al., 2013) are applied to the ground measured NO_2 before comparing with the modeled results due to the measurement artifacts in the heated molybdenum catalytic converter used by AQS NO_2 monitors.

The NOAA P-3 aircraft measurements (http://www.esrl.noaa.gov/csd/tropchem/2006TexAQS/) are available on 31 August, 11 September, 13 September, and 15 September 2006 in our modeling period. The NO_2 was measured by UV photolysis converter-chemiluminescence (Ryerson et al., 2000), and NO_y was measured by Au converter-chemiluminescence (Ryerson et al., 1999) aboard the P-3 aircraft, from ground to approximately 5km aloft and with a time resolution of 1-second; thus, hourly averaged P-3 NO_2 and NO_y are calculated to compare with the modeled data at corresponding time and grid cells.

2.5.3 NASA DC-8 flight NO_2 observations

The NO_2 measured by NASA DC-8 flights (http://www-air.larc.nasa.gov/cgi-bin/arcstat) during the Intercontinental Chemical Transport Experiment-North America (INTEX-NA) field campaign in 2004 (Singh et al., 2006) is used in this study to evaluate the modeled NO_2 vertical profile, especially in the upper troposphere. The DC-8 flight NO_2 measurements were made on a total of 18 days from 1 July to 14 August 2004, spanning from 7:00 to 20:00 CST with 1-second resolution. The NO_2 was measured by the Thermal Dissociation-Laser Induced Fluorescence (TD-LIF) instrument. TD-LIF measurements of NO_2 can be impacted by methyl peroxy nitrate

($CH_3O_2NO_2$) and HO_2NO_2 in a temperature-dependent manner; thus, corrections based on the method of Browne et al., (2011) are applied before comparing with the modeled profile. The modeled NO_2 in grid cells within the 36km domain are used to match the measurement data in space, and then all measurement data at each model layer are averaged over all measurement time to compare with the monthly 12-h (7:00-20:00LT) averaged modeled data at the corresponding layer. Although the measurements took place in 2004 and our modeling period is in 2006, we assume the inter-annual variation is insignificant because the upper tropospheric NO_2 is mainly contributed by natural sources and cross-tropopause transport.

3. Results and Discussion

3.1 Impact of GOES-derived photolysis rates on modeled NO_2 and O_3

The GOES-retrieved cloud fractions and broadband transmissivity as described in section 2.2 are used to adjust the photolysis rates in CAMx. To investigate the impact from GOES-derived photolysis rates, the differences of modeled ground-level NO_2 photolysis rate (J_{NO2}), NO_2, and O_3 between CAMx modeling with and without the GOES-retrieved cloud fractions and transmissivity are calculated.

Using GOES-observed clouds corrects the cloud underprediction issue in the current meteorological models (Pour-Biazar et al., 2007; Guenther et al., 2012; ENVIRON 2012), making J_{NO2} decreases over most of the domain in this study. While on the average there is a domain-wide reduction in J_{NO2}, the impact on O_3 production is not uniform (Figs. 2 and 3), mostly paired with the NO_x emission distributions. The general impact of using GOES observations is that where the J_{NO2} decreases, modeled NO_2 increases, and O_3 decreases (Figs. 2 and 3), indicating that slower photochemical activity inhibits O_3 formation and thus consumes less $NO_{2,}$ and vice versa. However, an exception occurs at places close to the Houston Ship Channel, showing that although the J_{NO2} decreases, modeled NO_2 still decreases (Fig. 3b) and O_3 slightly increases (Fig. 3c). This is probably caused by the availability of other pathways for consuming NO_x in the VOC-rich environment, and the inhibition of NO regeneration due to reduction in photochemical activity. The largest discrepancy of 80ppb in modeled O_3 occurs at 13:00 on 2 September 2006 over the DFW region during the modeling period. At that time, GOES-based modeling showed up to 6 times higher J_{NO2} (reaching approximately 36s^{-1}), and 10ppb lower NO_2 in this region (Fig. 2). However, the differences in modeled J_{NO2}, $NO_{2,}$ and O_3 are much more moderate on a monthly 8-h (10:00-18:00) averaged basis, reaching only up to 3s^{-1} for J_{NO2}, 0.6ppb for $NO_{2,}$ and 3ppb for $O_{3,}$ with largest discrepancies in the HGB region (Fig. 3). For the changes in O_3 sensitivities, approximately 6% less J_{NO2} on a domain-wide makes modeled O_3 overall less sensitive to NO_x emissions (Fig. 3d) and more sensitive to VOC emissions (Fig. 3e).

The modeled daily 8-h (10:00-18:00LT) NO_2 and O_3 using either satellite-derived or base model photolysis rates are evaluated by AQS measured data for the entire modeling period. The positive changes in spatiotemporal correlation (R^2) and negative changes in NMB and NME indicate that satellite-derived photolysis rates improved model performance (Fig. 4). For O_3 simulations (Fig. 4 right), the difference in R^2 increases 1% on average and reaches up to 7% on 26 August, while the differences in NMBs and NMEs decrease 1% on average and reach up to 10% on 11 September, suggesting the satellite-corrected photolysis rates improve the model performance in simulating ground O_3. However, NMB and NME for NO_2 simulations (Fig. 4 left) do not improve despite an increase in R^2, probably because other uncertainties in the model and measurements may have a larger impact on NO_2 performance.

3.2 Pseudodata test for the sector-based DKF inversion

A controlled pseudodata test was performed in Tang et al. (2013) to test the applicability of the DKF inversion to adjust the NO_x emission in each inversion region with the CAMx-DDM model. This showed that the DKF method adjusted the perturbed NO_x emission in each region accurately back to its base case. In this study, a similar controlled pseudodata test is conducted to test the applicability of the sector-based DKF inversion with CAMx-DDM.

The pseudodata test for the sector-based DKF inversion is conducted on 10 modeling days (13 August to 22 August), but the modeling results from the first 3 days are discarded to eliminate the model initialization error. A 7-day (16 August to 22 August) averaged modeled NO_2 VCDs at 13:00-14:00LT with the base case NO_x emission inventory is treated as a pseudo-observation, and the one using perturbed NO_x emissions in six emission sectors with known perturbation factors ranging from 0.5 to 2.0 (Fig. 6) is used as a priori case. As described in section 2.3, the area and non-road emission sources are considered as one sector (ARNR), and EGU point source is excluded from the inversion. The emission uncertainties are set to 50% for the non-EGU and lightning sectors and to 100% for the others. The measurement error for the pseudo-observation is set to 30%.

The pseudodata test results (Fig. 6 top) show that the a posteriori modeled NO_2 closely matches the base case modeled value, indicating the DKF inversion is capable of correcting the perturbed NO_x emissions in each emission sector. The sensitivity analysis results (Fig. 6 bottom) illustrate that the inversions are insensitive to both emission and observation error covariance matrices for the pseudo-cases.

3.3 A priori NO_2 VCDs

The a priori NO_x emission inventory used in this study is based on the TCEQ base case emission inventory with added lightning and aviation and doubled soil NO_x emissions (Tang et al., 2013). The reaction rate constant of the reaction NO_2 + OH in CB05 chemical mechanism is reduced by 25% based on Mollner et al. (2010); this tends to increase NO_x lifetime and transport to rural regions.

To evaluate the extent to which the addition of lightning and aviation NO_x closes the gap between observed and modeled NO_2 in the upper troposphere noticed by Napelenok et al. (2008), the modeled NO_2 vertical profile is compared with INTEX-NA DC-8 measured NO_2 profiles from the ground to the free troposphere. The comparison (Fig. 7 left) shows that CAMx with the a priori emission inventory strongly overestimates NO_2 near the ground, reasonably agrees with DC-8 NO_2 measurements from 1km to 5km, slightly overestimates NO_2 from 6km to 9km, and slightly underestimates NO_2 from 10km to 15km. The modeled NO_2 profile is further evaluated by the P-3 measured NO_2 from ground to 5km (Fig. 7 right), showing the same pattern of the overestimated surface NO_2 and good agreement with aircraft observations from 1km-5km. The injection of the aviation NO_x into a single model layer at altitude 6km to 9km rather than more broadly distributed vertically probably causes the overestimation of modeled NO_2 compared to DC-8 at that altitude (ENVIRON, 2013). A low bias of modeled NO_2, approximately 40ppt, exists in the upper troposphere, from 10km to 15km altitude, which is the CAMx model top layer. Similar low bias of the modeled NO_2 in the upper troposphere compared to the DC-8 measurement also has been found in Allen et al. (2012). Because the low bias in the upper troposphere may arise from model uncertainties other than those associated with emissions (Henderson et al., 2011; 2012), we follow the adjustment approach of Napelenok et al. (2008)

and add 40ppt NO_2 homogeneously to the top layer (10-15km) of the model results when computing the CAMx NO_2 VCDs.

Although the revised CB05 chemical mechanism and artificially added upper tropospheric NO_2 increase modeled NO_2 VCDs in the inversion region by an average of 13% (Supplement, Sect. 2), CAMx modeled NO_2 VCDs remain an average of 2×10^{14} molecules/cm^2 less than OMI observations in rural regions (Fig. 8c).

3.4 Top-down NO_x emissions constrained by DKF inversions

The DKF inversions with OMI NO_2 are performed to constrain NO_x emissions in each designated emission region and emission sector. To ensure sufficient spatial coverage, a monthly averaged OMI NO_2 VCD (13 August to 15 September) is calculated and paired with the corresponding modeled NO_2 VCD at satellite passing time (13:00-14:00LT). The DKF inversions are then conducted with 2116 data points covering every grid cell in the inversion region, and the hourly a priori NO_x emissions are adjusted iteratively until the inversion process converges.

3.4.1 Region-based DKF inversion

The region-based DKF inversion is conducted to adjust the NO_x emissions in each inversion region. The inversion results suggest to moderately adjust the a priori NO_x emissions in most regions with scaling factors ranging from 0.97 to 1.49 (Table 2) and increases NO_2 VCDs by 8% toward OMI measurement over the inversion region (Fig. 8d). Because this inversion is based on a new OMI-retrieved and an improved a priori NO_2 VCDs, the required adjustments in each inversion region are much lower compared to the results in Tang et al. (2013) with scaling factors ranging from 0.56 to 1.98 and 30% increased NO_2 VCDs.

The model performance is then evaluated by the ground and aircraft measurements. The DKF inversion adjusts DFW NO_x emissions by only 3%, while it adds 49% to BPA emissions and less than 15% to other urban regions. The NMB and NME of the a posteriori modeled NO_2 VCDs decrease in every urban area and are reduced from -0.11 to -0.05 and from 0.17 to 0.16 overall compared to OMI. The spatial correlations between monthly averaged OMI and CAMx NO_2 VCDs (R^2) are improved only in the BPA and Austin and San Antonio areas, but the overall region-wide performance is improved (Table 3). The modeled NO_2 with a priori NO_x emissions overpredicts ground-level NO_2 (Table 4); hence, the increase in NO_x emissions at most urban places suggested by the inversion actually deteriorates the ground-level NO_2 simulations in all urban areas except in the DFW region. The modeled NMB and NME of ground O_3 are reduced in the HGB and BPA regions, but not in DFW, probably because the increased NO_x in the first two regions titrates more ground O_3 at night and inhibits O_3 formation during the day, decreasing the O_3 concentrations which are already overestimated in the a priori simulation (Table 6). No improvements of model performance are found in simulating P-3 observed NO_2 and NO_y using the inverted NO_x emissions.

Applying a single scaling factor to an entire inversion region may not well capture the NO_x spatial distributions (Tang et al., 2013). Since DDM can also track the spatial relationship between modeled NO_2 concentrations and NO_x emissions in each emission sector, a sector-based DKF inversion can potentially serve as an alternative approach to constrain NO_x emissions in order to have more heterogeneous adjustments in each inversion region.

3.4.2 Sector-based DKF inversion

The sector-based DKF inversion is first conducted on six NO_x emission sectors: area and nonroad (ARNR), on-road, biogenic, aviation, lightning, and non-EGU points (Case I). The scaling factors generated by the inversion ranges from 0.54 to 4.10, with the largest scale-down in the ARNR sector and the largest scale-up in the aviation sector. The inversion reduces NO_x emission in the biogenic sector by 30% from the a priori inventory which had doubled soil NO_x from the base model. The inversion leaves on-road, lightning, and non-EGU points sectors nearly unchanged, applying less than 4% adjustments (Table 2). The NO_2 VCD is increased by only 6% toward OMI measurement over the inversion region in this case. Most of the increase in NO_2 VCDs occurs in rural areas, and some declines occur in urban areas (Fig 8e).

The NO_x emission in each inversion region is recalculated after applying adjustments to each emission sector, and model performance is evaluated by the ground and aircraft measurements. The scaling factors in each region now are different and closer to 1 than those generated by the region-based inversion, ranging from 0.86 in NE TX to 1.17 in DFW. The modeled NMB and NME in simulating OMI NO_2 are all decreased in five urban areas. Within the inversion region, the overall modeled NMB and NME are reduced from -0.11 to -0.04 and from 0.17 to 0.14, respectively using inverted NO_x emissions (Table 3). The 50% cut in the ARNR sector helps to improve the model performance in simulating ground-level NO_2 and O_3 which had been overestimated using a priori NO_x emissions. The inverted NO_x emissions decrease modeled NMB and NME in all five urban areas and overall decrease NMB by 0.25 and 0.04, and NME by 0.13 and 0.04 in simulating ground-level NO_2 and O_3, respectively (Table 4 and Table 6). The model performance is also improved compared against P-3 measurements. For NO_2, NMB is reduced from 0.09 to -0.02, and NME is reduced by 0.09. For NO_y, NMB is reduced by 0.16 and NME is reduced by 0.11 (Table 5). The scaled-down ground NO_x emissions lead to a 2-5 ppb lower modeled 8-h (10:00-18:00LT) ground O_3 and make O_3 formation chemistry less sensitive to the VOC emissions, with reduction of 1-3ppb sensitivity coefficients over the inversion region. The O_3 sensitivity to NO_x emissions also decreases by approximately 1-2ppb over most of the inversion region; however, the O_3 formation chemistry in the urban cores of the DFW, HGB, and Austin and San Antonio regions shifts toward being more NO_x-limited, leading to a 1-3 ppb increase of O_3 sensitivity to NO_x emissions (Fig. 9).

Although the inversion improves the model performance, the sensitivity analysis (Supplement, Sect. 3) shows that the aviation and ARNR sectors are relatively responsive to the emission uncertainty values and offset each other (Fig. S2), indicating the DKF inversion may not be capable of fully distinguishing these two emission sectors. Therefore, the aviation source is then merged with ARNR and the DKF inversion is re-conducted on five emission sectors: area, nonroad, and aviation (ARNRAV), on-road, biogenic, lightning, and non-EGU points (Case II). In case II, the inversion results are more stable and insensitive to the emission uncertainties in each emission sector (Fig. S2). However, the inversion tends to scale up all three source categories in the ARNRAV sector together by 50% to compensate for the rural NO_2 gap. The inversion reduces on-road and biogenic NO_x emissions by 12% and 16%, respectively. The adjustments for the lightning and non-EGU points sectors are still less than 4% (Table 2). On the region basis, the inversion tends to increase NO_x emissions in all regions with increments ranging from 1% in the Austin and San Antonio region to 18% in the NE TX region; it thus increases the modeled NO_2 VCDs by 7% on average. The inversed NO_2 VCD in this case is very similar to that from the region-based inversion (Fig. 8f). The model performance of simulating OMI NO_2 VCDs is improved and similar to the results from case I (Table 3). However, unlike case I, no improvements are found in simulating ground measured NO_2 and O_3 and P-3-measured NO_2 and NO_y using the inverted NO_x emissions in case II (Table 4-6). Because the ground NO_x emissions are increased in this case, the inversion impacts the O_3 simulations in the opposite direction than in case I. The modeled 8-h ground O_3 increases by around 2ppb and becomes more sensitive to both NO_x and VOC emissions over most of the inversion region; however, the O_3 formation chemistry shifts toward being more VOC-limited in DFW and HGB (Fig. 9).

4. Conclusions

Satellite-derived photolysis rates and NO_x emissions are both applied to a Texas SIP modeling episode to investigate the capabilities of using satellite data to enhance state-level O_3 regulatory modeling. Results show that the ground-level O_3 simulations are improved with reductions of modeled NMB from 0.42 to 0.37 and modeled NME from 0.50 to 0.45 by using GOES-derived photolysis rates and sector-based DKF (case I) with OMI NO_2 inverted NO_x emission inventory (Table 6). The GOES-derived photolysis rates and OMI-constrained NO_x emissions decrease monthly averaged 8-h O_3 concentrations by 2-5ppb over the entire inversion region and turn O_3 formation chemistry toward being less sensitive to NO_x and VOC emissions over most of inversion areas, while being more NO_x sensitive in the two O_3 nonattainment areas, DFW and HGB (Fig. 10).

Applying GOES-retrieved cloud coverage and transmissivity reduce the modeled photolysis rates over most of the domain, leading to less photochemical activity and O_3 production and shifting O_3 formation chemistry toward being less sensitive to NO_x emissions, except in the DFW region where modeled photolysis rates are increased by the GOES retrieval, leading to impacts in the opposite direction. In comparing with the AQS ground measurements, the GOES-derived photolysis rates improve the ground-level O_3 simulations but not the NO_2 simulations, indicating other model errors may dominate the accuracy of model performance in simulating ground-level NO_2. The GOES-retrieved clouds applied here adjusted only the modeled photolysis rates, while modeled clouds continued to drive the dynamics and aqueous phase chemistry. This inconsistency in the placement of clouds is similar to the approach of a previous study (Pour-Biazar et al., 2007). Thus, this work demonstrates a sensitivity study of using satellite-derived photolysis rates on model performance rather than a full integration of satellite-observed clouds into all aspects of the model. Future work could extend the use of GOES-retrieved clouds to also correct model dynamics and aqueous phase chemistry and investigate their impacts on NO_x and O_3 modeling.

The DKF inversion approach has been successfully incorporated with the CAMx-DDM model and was conducted on both region-based and sector-based NO_x emissions. A controlled pseudodata test conducted on the sector-based DKF inversion confirmed that it accurately captures known perturbations in NO_x emission sectors. In addition to implementing lightning and aviation NO_x emissions in the upper troposphere and doubling soil NO_x emissions from the ground, the NO_x lifetime is increased by reducing 25% the reaction rate constant of the reaction $OH + NO_{2.}$ The upper tropospheric NO_2 underestimation is further eliminated by adding a 40ppt homogenous NO_2 layer in the model top. On the other hand, the high resolution OMI retrieval with a priori profile from the nested GEOS-Chem simulation further enhances NO_2 in urban areas and reduces NO_2 in rural. However, the comparison still shows that the OMI has higher NO_2 VCDs than CAMx in rural areas, by around 2×10^{14} molecules/cm^2. It is not clear that the discrepancy between OMI and CAMx in rural areas is caused by uncertainties in NO_x emission inventory or errors in OMI retrieval and other model uncertainties. The OMI NO_2 retrieval can be further improved by using the finer resolution terrain and albedo data (Russell et al., 2011) and observed vertical profiles from aircraft spiral measurements in the recent DISCOVER-AQ Houston measurement campaign (Crawford et al., 2014). The accuracy of CAMx modeled NO_2 VCDs can benefit from further improving the modeled chemical and transport processes (ENVIRON 2013), such as updating NO_x recycling process to increase NO_x lifetime, or adding cross-tropopause transport processes to allow more stratospheric NO_2 penetrate to upper troposphere. This may obtain better spatial distribution of modeled NO_2 rather than adding a homogeneous layer at top to compensate the model deficiency.

The region-based DKF inversion still over scales NO_x emissions in urban areas to compensate for the rural NO_2 differences because the NO_2 VCDs gap in rural areas is not eliminated, leading to 10-50% increase of NO_x emissions at most regions and worsening the ground-level O_3 simulations; however, the scaling factors generated in this study are much more moderate than those were found in Tang et al. (2013). The sector-based DKF inversion (case I) takes the aviation source to compensate the NO_2 gap in rural area, probably because its relatively spread-out emission pattern over rural area corresponds with the NO_2 discrepancy distributions, leading to appropriate adjustments in the ground emissions and improving both ground-level NO_2 and O_3 simulations; however, the aviation source is unrealistically adjusted by applying a suggested factor of 4 to its base value, and the adjustments offset the area and nonroad sector with varying emission uncertainties in the sensitivity analysis. Although merging the aviation source into the area and nonroad emission sector makes the inversion (case II) more stable, the large scaling factor for the aviation sector is now shared with area and nonroad emissions, leading to area and nonroad NO_x emissions being scaled up by 50%. Thus, the model performance in ground-level NO_2 and O_3 simulations is deteriorated and is even worse than the results generated from the region-based inversion. The lightning NO_x emissions seem to be well estimated and are adjusted little by the inversion. However, it may also indicate that the OMI retrieved NO_2 is insensitive to the lightning source, most probably due to the NO_x partitioning predominantly to NO in the upper troposphere and the clear-sky cloud screening criterion used in the OMI data processing. The NO_2 discrepancy between OMI and CAMx drives the DKF inversion and is assumed to be mostly contributed by the uncertainties in the NO_x emission inventory. However, findings from this study indicate that if the uncertainty in the a priori NO_x emissions is low, errors in the satellite retrieval and model itself cannot be neglected, making the inversion less capable of reducing the uncertainties in the bottom-up NO_x emission inventory.

The region-based DKF inversion applies a single scaling factor to each inversion region, and assumes the a priori emission pattern in each inversion region is correct, causing deterioration of the model performance in this case. While the sector-based DKF inversion applies a single scaling factor to each emission sector, that leads to more heterogeneous adjustments in each inversion region and relatively better modeling results than those from the region-based inversion. However, the sector-based inversion assumes the spatial distribution of NO_x emissions in each sector is accurately estimated in the bottom-up NO_x emission inventory, which is also a simplification. For example, TCEQ recently developed a single-day aviation emission inventory using the Advanced Emission Model (AEM3) for the new Rider 8 modeling domain, which has more accurate flight profile and distributes emissions more broadly in the vertical direction, leading to the spatial pattern of NO_x emissions somewhat different than that obtained from EDGAR (ENVIRON 2013). In addition, the newly developed Berkeley-Dalhousie

Soil NO_x Parameterization (BDSNP) scheme (Hudman et al., 2012) recently was implemented into the CMAQ model to estimate soil NO_x emissions, showing large spatial and temporal differences compared to those estimated by the YL95 scheme over eastern Texas. All these changes described above in the a priori NO_x emission inventory may have significant impact on the sector-based inversion results.

The direct scaling inversion (Supplement, Sect. 4) using PAMS measured VOCs improves the model performance in simulating five chosen VOC species and indicates the TCEQ VOC emission inventory used in HGB SIP modeling is now much better than the previous reported emissions with values off by an order of magnitude. However, the inverted VOC emissions have insignificant impact on the ground-level NO_2 and O_3 simulations, probably because of the limited spatial coverage of the PAMS measurement sites and most VOC-saturated conditions in the inversion region. Future work could explore the capabilities of using satellite-observed formaldehyde data to constrain the Texas isoprene or even other anthropogenic VOC emissions (Defour et al., 2009; Curci et al., 2010).

The statistical results show that although the modeled NMB and NME are reduced, OMI-constrained NO_x emissions barely improve the spatiotemporal correlations (R^2) with ground-measured NO_2 and O_3, indicating that either applying the scaling factors generated at the OMI passing time is unable to reduce the emission uncertainty at each hour or the current OMI resolution is insufficient to capture the spatial distributions of the NO_x emission pattern. The future launch of NASA Tropospheric Emission: Monitoring of Pollution (TEMPO) geostationary satellite (Streets et al., 2013) could help address these shortcomings by providing a temporal resolution down to an hour and a spatial resolution down to 4km×4km measurement.

Acknowledgements. Funding for this research was provided by the U.S. NASA Research Opportunities in Space and Earth Sciences (ROSES) grant NNX10AO05G and by the NASA Air Quality Applied Science Team. The authors thank Jim McKay and Ron Thomas at TCEQ for providing emission inputs and insightful discussions about the TCEQ emission inventory, Gary Wilson and Greg Yarwood at ENVIRON for CAMx support, Ron Cohen at UC-Berkeley for the INTEX-NA DC-8 NO_2 measurement, and Tom Ryerson, Carsten Warneke, and Joost de Gouw at NOAA for the P-3 NO_2, NO_y and VOC measurements.

References

Allen, D. J., Pickering, K. E., Pinder, R. W., Henderson, B. H., Appel, K. W., and Prados, A.: Impact of lightning-NO on eastern United States photochemistry during the summer of 2006 as determined using the CMAQ model. Atmos. Chem. Phys., 12, 1737-1758, 2012.

Boersma, K. F., Eskes, H. J., Veefkind, J. P., Brinksma, E. J., van der A, R. J., Sneep, M., van der Oord, G. H. J., Levelt, P. F., Stammes, P., Gleason, J. F., and Bucsela, E. J.: Near-real time retrieval of tropospheric NO_2 from OMI. Atmos. Chem. Phys., 112, 2103–2118, 2007.

Browne, E. C., Perring, A. E., Wooldridge, P. J., Apel, E., Hall, S. R., Huey, L. G., Mao, J., Spencer, K. M., St. Clair, J. M., Weinheimer, A. J., Wisthaler, A., and Cohen, R. C.: Global and regional effects of the photochemistry of CH3O2NO2: Evidence from ARCTAS. Atmos. Chem. Phys., 11, 4209–4219, 2011.

Bucsela, E. J., Krotkov, N. A., Celarier, E. A., Lamsal, L. N., Swartz, W. H., Bhartia, P. K., Boersma, K. F., Veefkind, J. P., Gleason, J. F., and Pickering, K. E.: A new stratospheric and tropospheric NO_2 retrieval algorithm for nadir-viewing satellite instruments: applications to OMI. Atmos. Meas. Tech., 6, 2607–2626, 2013.

Chai, T., Carmichael, G. R., Tang, Y., Sandu, A., Heckel, A., Richter, A., and Burrows, J. P.: Regional NO_x emission inversion through a four-dimensional variational approach using SCIAMACHY tropospheric NO_2 column observations. Atmos. Environ., 43, 5046-5055, 2009.

Chang, J. S., Brost, R. A., Isaksen, I. S. A., Madronich, S., Middleton, P., Stockwell, W. R., and Walcek, C. J.: A 3-dimensional Eulerian acid deposition model - Physical concepts and formulation. J. Geophys. Res., 92, D12, 14681-14700, 1987.

Cohan, D. S., Koo, B., and Yarwood, G.: Influence of uncertain reaction rates on ozone sensitivity to emissions in Houston. Atmos. Environ., 44, 3101-3109, 2010.

Crawford, J., Pickering, K., Kleb, M., and Chen, G.: DISCOVER-AQ: Overall objectives and overview of Houston operations during September 2013, presented in 6th AQAST meeting, Houston, TX, 16 January, 2014.

Curci, G., Palmer, P. I., Kurosu, T. P., Chance, K., and Visconti, G.: Estimating European volatile organic compound emissions using satellite observations of formaldehyde from the Ozone Monitoring Instrument. Atmos. Chem. Phys., 10, 11501–11517, 2010.

Daum, P. H., Kleinman, L. I., Springston, S. R., Nunnemacker, L. J., Lee, Y-N., Weinstein-Lloyd, J., Zheng, J., and Berkowitz, C. M.: Origin and properties of plumes of high ozone observed during Texas 2000 Air Quality Study (TEXAQS 2000). Geophys. Res. Lett., 109, D17306, doi: 10.1029/2003JD004311, 2004.

Deguillaume, L., Beekmann, M., and Menut, L.: Bayesian Monte Carlo analysis applied to regional-scale inverse emission modeling for reactive trace gases. J. Geophys. Res., 112, D02307, doi:10.1029/2006JD007518, 2007.

Digar, A. and Cohan, D. S.: Efficient characterization of pollutant-emission response under parametric uncertainty. Environ. Sci. Technol., 44, 6724-6730, 2010.

Digar, A., Cohan, D. S., and Bell, M. L.: Uncertainties influencing health-based prioritization of ozone abatement strategies. Environ. Sci. Technol., 45, 7761-7767, 2011.

Dufour, G., Wittrock, F., Camredon, M., Beekmann, M., Richter, A., Aumont, B., and Burrows, J. P.: SCIAMACHY formaldehyde observations: constraint for isoprene emission estimates over Europe? Atmos. Chem. Phys., 9, 1647–1664, 2009.

ENVIRON: Boundary Conditions and Fire Emissions Modeling, Final Report to the Texas Commission on Environmental Quality. ENVIRON International Corporation, Novato, CA, 2008.

ENVIRON: CAMx Users' Guide, version 5.30. ENVIRON International Corporation, Novato, CA, 2010.

ENVIRON: Improved the Biogenic Emission Inventories across the West, Final Report to the Western Governors' Association. ENVIRON International Corporation, Novato, CA, 2012.

ENVIRON. Continuation on Use of Satellite Nitrogen Dioxide (NO_2) Data. Final Report to the Texas Commission on Environmental Quality. ENVIRON International Corporation, Novato, CA, 2013.

Eskes, H. J. and Boersma, K. F.: Averaging kernels for DOAS total column satellite retrievals. Atmos. Chem. Phys., 3, 1285–1291, 2003.

Fine, J., Vuilleumier, L., Reynolds, S., Roth, P., Brown, N.: Evaluating uncertainties in regional photochemical air quality modeling. Annu. Rev. Env. Resour. 28, 59-106, 2003.

Gonzales, M. and Williamson, W.: Updates on the National Ambient Air Quality Standards and the State Implementation Plans for Texas, presented in TCEQ Trade Fair, Austin, TX, 4 May, 2011.

Grell, G. A., Dudhia, J., and Stauffer, D.: A description of the fifth-generation PennState/NCAR mesoscale model (MM5), NCAR Technical Note, NCAR/TN 398+SR, Boulder, Colorado, 1994.

Guenther, A. B., Jiang, X., Heald, C. L., Sakulyanontvittaya, T., Duhl, T., Emmons, L. K., and Wang, X.: The Model of Emission of Gases and Aerosols from Nature version 2.1 (MEGAN2.1): an extended and updated framework for modeling biogenic emissions. Geosci. Model Dev., 5, 1471-1492, 2012.

Haines, S. L., Suggs, R. J., and Jedlovec, G. J.: The Geostationary Operational Environmental Satellite (GOES) product generation system. NASA Tech. Memo., TM-2004-213286. NASA, Huntsville, Alabama, 2004.

Hanna, S. R., Lu, Z., Frey, H. C., Wheeler, N., Vukovich, J., Arumachalam, S., and Fernau, M.:

Uncertainties in predicted ozone concentration due to input uncertainties for the UAM-V photochemical grid model applied to the July 1995 OTAG domain. Atmos. Environ., 35, 891-903, 2001.

Henderson, B. H., Pinder, R. W., Crooks, J., Cohen, R. C., Hutzell, W. T., Sarwar, G., Goliff, W. S., Stockwell, W. R., Fahr, A., Mathur, R., Carlton, A. G., and Vizuete, W.: Evaluation of simulated photochemical partitioning of oxidized nitrogen in the upper troposphere. Atmos. Chem. Phys., 11, 275-291, 2011.

Henderson B. H, Pinder, R. W., Crooks, J., Cohen, R. C., Carlton, A. G., Pye, H. O. T., and Vizuete, W.: Combining Bayesian methods and aircraft observations to constrain the HO + NO2 reaction rate. Atmos. Chem. Phys., 12, 653–667, 2012.

Hudman, R. C., Jacob, D. J., Turquety, S., Leibensperger, E. M., Murray, L. T., Wu, S., Gilliland, A. B., Avery, M., Bertram, T. H., Brune, W., Cohen, R. C., Dibb, J. E., Flocke, F. M., Fried, A., Holloway, J., Neuman, J. A., Orville, R., Perring, A., Ren, X., Sachse, G. W., Singh, H. B., Swanson, A., Wooldridge, P. J.: Surface and lightning sources of nitrogen oxides over the United States: Magnitudes, chemical evolution, and outflow. J. Geophys. Res., 112, D12S05, doi:10.1029/2006JD007912, 2007.

Hudman, R. C., Russell, A. R., Valin, L. C., and Cohen, R. C.: Interannual variability in soil nitric oxide emissions over the United States as viewed from space. Atmos. Chem. Phys., 10, 9943–9952, 2010.

Hudman, R. C., Moore, N. E., Mebust, A. K., Martin, R. V., Russell, A. R., Valin, L. C., and Cohen, R. C.: Steps towards a mechanistic model of global soil nitric oxide emissions: implementation and space based-constraints. Atmos. Chem. Phys., 12, 7779–7795, 2012.

Jaeglé, L., Steinberger, L., Martin, R. V., and Chance, K.: Global partitioning of NO_x sources using satellite observations: Relative roles of fossil fuel combustion, biomass burning and soil emissions. Faraday Discuss., 130, 407-423, 2005.

Kaynak, B., Hu, Y., Martin, R. V., Russell, A. G., Choi, Y., and Wang, Y.: The effect of lightning NO_x production on surface ozone in the continental United States. Atmos. Chem. Phys., 8, 5151–5159, 2008.

Kim, S. W., McKeen, S. A., Frost, G. J., Lee, S.-H., Trainer, M., Richter, A., Angevine, W.M., Atlas, E., Bianco, L., Boersma, K. F., Brioude, J., Burrows, J. P., de Gouw, J., Fried, A., Gleason, J., Hilboll, A., Mellqvist, J., Peischl, J., Richter, D., Rivera, C., Ryerson, T., te Lintel Hekkert, S., Walega, J., Warneke, C., Weibring, P., and Williams, E.: Evaluations of NO_x and highly reactive VOC emission inventories in Texas and their implications for ozone plume simulations during the Texas Air Quality Study 2006. Atmos. Chem. Phys., 11, 11361-11386, 2011.

Kleinman, L. I., Daum, P. H., Imre, D., Lee, Y-N., Nunnemacker, L. J., and Springston, S.R.: Ozone production rate and hydrocarbon reactivity in five urban areas: A case of high ozone concentration in Houston. Geophys. Res. Lett., 29, 1467 10.1029/2001GL014569, 2002.

Konovalov, I. B., Beekmann, M., Richter, A., and Burrows, J. P.: Inverse modeling of the spatial distribution of NO_x emissions on a continental scale using satellite data. Atmos. Chem. Phys., 6, 1747–1770, 2006.

Konovalov, I. B., Beekmann, M., Burrows, J. P., and Richter, A.: Satellite measurement based estimates of decadal changes in European nitrogen oxides emissions. Atmos. Chem. Phys., 8, 2623–2641, 2008.

Kurokawa, J., Yumimoto, K., Uno, I., and Ohara, T.: Adjoint inverse modeling of NO_x

emissions over eastern China using satellite observations of NO_2 vertical column densities. Atmos. Environ., 43(11), 1878-1887, 2009.

Lamsal, L. N., Martin, R.V., van Donkelaar, A., Steinbacher, M., Celarier, E. A., Bucsela, E., Dunlea, E. J., and Pinto, J. P.: Ground level nitrogen dioxide concentrations inferred from the satellite borne Ozone Monitoring Instrument. J. Geophys. Res., 113, D16308, doi:10.1029/2007JD009235, 2008.

Lamsal, L. N., Krotkov, N. A., Celarier, E. A., Swartz, W. H., Pickering, K. E., Bucsela, E. J., Martin, R. V., Philip, S., Irie, H., Cede, A., Herman, J., Weinheimer, A., Szykman, J. J., and Knepp, T. N.: Evaluation of OMI operational standard NO_2 column retrievals using in situ and surface-based NO_2 observations. Atmos. Chem. Phys. Discuss., 14, 14519–14573, 2014.

Levelt, P. F., Hilsenrath, E., Leppelmeier, G.W., van den Oord, G. H. J., Bhartia, P. K., Tamminen, J., de Haan, J. F., and Veefkind, J. P.: Science objective of the Ozone Monitoring Instrument. IEEE. T. Geosci. Remote., 44, 1199–1208, 2006.

Levelt, P. F., van den Oord, G. H. J., Dobber, M. R., Malkki, A., Visser, H., de Vries, J., Stammes, P., Lundell, J. O. V., and Saari, H.: The Ozone Monitoring Instrument. IEEE. T. Geosci. Remote., 44, 1093–1101, 2006.

Lin, J. T., McElroy, M. B., and Boersma, K. F.: Constraint of anthropogenic NO_x emissions in China from different sectors: a new methodology using multiple satellite retrievals. Atmos. Chem. Phys., 9(5), 19205-19241, 2010.

Lin, J. T., Liu, Z., Zhang, Q., Liu, H., Mao, J., and Zhuang, G.: Modeling uncertainties for tropospheric nitrogen dioxide columns affecting satellite-based inverse modeling of nitrogen oxides emissions. Atmos. Chem. Phys., 12, 12255-12275, 2012.

Madronich, S.: Photodissociation in the atmosphere 1. Actinic flux and the effects of ground reflections and clouds. J. Geophys. Res., 92, D8, 9740-9752, doi: 10.1029/JD092iD08p09740, 1987.

Martin, R. V., Jacob, D. J., Chance, K., Kurosu, T. P., Palmer, P. I., and Evans, M. J.: Global inventory of nitrogen oxide emissions constrained by space-based observations of NO_2 columns. J. Geophys. Res., 108(D17), 4537, doi:10.1029/2003JD003453, 2003.

Martin, R. V., Sauvage, B., Folkins, I., Sioris, C. E., Boone, C., Bernath, P., and Ziemke, J.: Space-based constraints on the production of nitric oxide by lightning. J. Geophys. Res., 112, D09309, doi: 10.1029/2006JD007831, 2007.

Mollner, A. K., Valluvadasan, S., Feng, L., Sprague, M. K., Okumura, M., Milligan, D. B., Bloss, W. J., Sander, S. P., Martien, P. T., Harley, R. A., McCoy, A. B., and Carter, W. P. L.: Rate of gas phase association of hydroxyl radical and nitrogen dioxide. Science, 330, 646-649, doi:10.1126/science.1193030, 2010.

Müller, J. F. and Stavrakou, T.: Inversion of CO and NO_x emissions using the adjoint of the IMAGES model. Atmos. Chem. Phys., 5, 1157-1186, 2005.

Napelenok, S. L., Pinder, R. W., Gilliland, A. B., and Martin, R. V.: A method for evaluating spatially-resolved NO_x emissions using Kalman filter inversion, direct sensitivities, and space-based NO_2 observations. Atmos. Chem. Phys., 8, 5603-5614, 2008.

NCAR. 2011. The Tropospheric Visible and Ultraviolet (TUV) Radiation Model web page. National Center for Atmospheric Research, Atmospheric Chemistry Division, Boulder, Colorado, http://cprm.acd.ucar.edu/Models/TUV/index.shtml, last access: September 2014.

Pour-Biazar, A., McNider, R. T., Roselle, S. J., Suggs, R., Jedlovec, G., Byun, D. W., Kim, S., Lin, C. J., Ho, T. C., Haines, S., Dornblaser, B., and Cameron, R.: Correcting photolysis rates on the basis of satellite observed clouds. J. Geophys. Res., 112, D10302, doi: 10.1029/2006JD007422, 2007.

Prinn, R. G.: Measurement equation for trace chemicals in fluids and solution of its inverse, in Inverse Methods in Global Biogeochemical Cycles, vol. 114, edited by Kasibhatla, P., Heimann, M., Rayner, P., Mahowald, N., Prinn, R. G., and Hartley, D. E., pp. 3-18, AGU, Washington, D.C., 2000.

Rappenglück, B., Perna, R., Zhong, S., and Morris, G.A.: An analysis of the vertical structure of the atmosphere and the upper-level meteorology and their impact on surface ozone levels in Houston, Texas. J. Geophys. Res., 113, D17315, doi: 10.1029/2007JD009745, 2008.

Ryerson, T. B., Trainer, M., Angevine, W. M., Brock, C. A., Dissly, R. W., Fehsenfeld, F. C., Frost, G. J., Goldan, P. D., Holloway, J. S., Hubler, G., Jakoubek, R. O., Kuster, W. C., Neuman, J. A., Nicks Jr., D. K., Parrish, D. D., Roberts, J. M., and Sueper, D. T.: Effect of petrochemical industrial emissions of reactive alkenes and NO_x on tropospheric ozone formation in Houston, Texas. J. Geophys. Res., 108 D084249, doi:10.1029/2002JD003070, 2003.

Rodgers, C. D.: Inverse methods for atmospheric sounding theory and practice, 1st ed., World Scientific, Singapore, 2000.

Russell, A. R., Perring, A. E., Valin, L. C., Hudman, R. C., Browne, E. C., Min, K-E., Wooldridge, P. J., and Cohen, R. C.: A high spatial resolution retrieval of NO_2 column densities from OMI: method and evaluation, Atmos. Chem. Phys., 11, 8543-8554, 2011.

Ryerson, T. B., Huey, L. G., Knapp, K., Neuman, J. A., Parrish, D. D., Sueper, D. T., and Fehsenfeld, F. C.: Design and initial characterizationof an inlet for gas-phase NOy measurements from aircraft. J. Geophys. Res., 104, 5483–5492, doi:10.1029/1998JD100087, 1999.

Ryerson, T. B., Williams, E. J., and Fehsenfeld, F. C.: An efficient photolysis system for fast-response NO2 measurements. J. Geophys. Res., 105, 26, 447–461, doi:10.1029/2000JD900389, 2000.

Schumann, U. and Huntrieser, H.: The global lightning-induced nitrogen oxides source. Atmos. Chem. Phys., 7, 3823-3907, 2007.

Seinfeld, J. H. and Pandis, S. N.: Atmospheric chemistry and physics. John Wiley & Sons, INC. New Jersey, 2006.

Simon, H., Baker, K. R., and Phillips, S.: Compilation and interpretation of photochemical model performance statistics published between 2006 and 2012. Atmos. Environ., 61, 124–139, 2012.

Singh, H. B., Brune, W. H., Crawford, J. H., Jacob, D. J., and Russell, P. B.: Overview of the summer 2004 intercontinental chemical transport experiment – North America (INTEX-A). J. Geophys. Res., 111, D24S01, doi:10.1029/2006JD007905, 2006.

Stavrakou, T., Müller, J.-F., Boersma, K. F., van der A, R. J., Kurokawa, J., Ohara, T., and Zhang, Q.: Key chemical NO_x sink uncertainties and how they influence top-down emissions of nitrogen oxides. Atmos. Chem. Phys., 13, 9057–9082, 2013.

Stephens, G. L.: Radiation profiles in extended water clouds. II: Parameterization schemes. J. Atmos. Sci., 35(11), 2123– 2132, 1978.

Streets, D. G., Canty, T., Carmichael, G. R., de Foy, B., Dickerson, R. R., Duncan, B. N., Edwards, D. P., Haynes, J. A., Henze, D. K., Houyoux, M. R., Jacob, D. J., Krotkov, N. A., Lamsal, L. N., Liu, Y., Lu, Z-F., Martin, R. V., Pfister, G. G., Pinder, R. W., Salawitch, R. J., and Wecht, K. J.: Emissions estimation from satellite retrievals: A review of current capability. Atmos. Environ., 77, 1011–1042, 2013.

Tang, W., Cohan, D. S., Lamsal, L.N., Xiao, X., and Zhou, W.: Inverse modeling of Texas NO_x emissions using space-based and ground-based NO_2 observations. Atmos. Chem. Phys., 13, 11005-11018, 2013.

TCEQ.: Houston-Galveston-Brazoria Attainment Demonstration SIP Revision for the 1997 Eight-Hour Ozone Standard, Austin, TX, 2010.

TCEQ.: Dallas-Fort Worth Attainment Demonstration SIP Revision for the 1997 Eight-hour Ozone Standard Non-attainment Area, Austin, TX, 2011.

Xiao, X., Cohan, D. S., Byun, D. W., and Ngan, F.: Highly nonlinear ozone formation in the Houston region and implications for emission controls. J. Geophys. Res., 115, D23309, doi:10.1029/2010JD014435, 2010.

Yienger, J. J. and Levy, H.: Empirical-model of global soil-biogenic NO_x emissions. J. Geophys. Res., 100(D6), 11447-11464. doi: 10.1029/95JD00370, 1995.

Zhao, C. and Wang, Y.: Assimilated inversion of NO_x emissions over east Asia using OMI NO_2 column measurements. Geophys. Res. Lett., 36, L06805, doi:10.1029/2008GL037123, 2009.

Zhou, W., Cohan, D. S., and Henderson, B. H.: Slower ozone production in Houston, Texas, following emission reductions: evidence from Texas Air Quality Studies in 2000 and 2006. Atmos. Chem. Phys., 12, 2777-2788, 2014.

Zyrichidou, I., Koukouli, M. E., Balis, D., Markakis, K., Poupkou, A., Katragkou, E., Kioutsioukis, I., Melas, D., Boersma, K. F., van Roozendael, M.: Identification of surface NO_x emission sources on a regional scale using OMI NO_2. Atmos. Environ., 101, 82-93, 2015.

Table 1. NO_x emission rates for seven sectors in seven inversion regions (tons/day).

Source Region	Area	On-road	Non-road	Biogenic	Aviation	Lightning	Non-EGU points	EGU	Total
HGB	28 (6%)	159 (36%)	71 (16%)	10 (2%)	28 (6%)	21 (5%)	92 (21%)	29 (7%)	438
DFW	35 (8%)	152 (37%)	77 (19%)	60 (14%)	44 (11%)	23 (6%)	19 (5%)	6 (1%)	416
BPA	8 (8%)	24 (24%)	7 (7%)	2 (2%)	3 (3%)	8 (8%)	40 (40%)	8 (8%)	101
NE Texas	43 (25%)	34 (20%)	28 (16%)	2 (1%)	3 (2%)	14 (8%)	9 (5%)	41 (24%)	174
Austin and San Antonio	9 (3%)	113 (37%)	37 (12%)	72 (24%)	12 (4%)	5 (2%)	21 (7%)	34 (11%)	303
N Rural	82 (11%)	161 (21%)	103 (13%)	142 (19%)	51 (7%)	94 (12%)	39 (5%)	91 (12%)	763
S Rural	85 (13%)	123 (18%)	79 (12%)	176 (26%)	30 (4%)	61 (9%)	61 (9%)	57 (8%)	672
Total	290 (10%)	766 (27%)	402 (14%)	464 (16%)	171 (6%)	226 (8%)	281 (10%)	266 (9%)	2866

Note: percentage indicates the apportionment of each emission sector to the regional total.

Table 2. Scaling factors of region-based and sector-based inversions.

Region-based inversion		Sector-based inversion I		Sector-based inversion II	
Emission region	Scaling factor (unitless)	Emission sector	Scaling factor (unitless)	Emission sector	Scaling factor (unitless)
HGB	1.11	Area	0.54	Area	1.49
DFW	0.97	Non-road	0.54	Non-road	1.49
BPA	1.49	On-road	1.03	On-road	0.88
NE Texas	1.10	Biogenic	0.71	Biogenic	0.84
Austin and San Antonio	1.15	Aviation	4.10	Aviation	1.49
N rural	1.24	Lightning	0.98	Lightning	1.03
S rural	0.98	Non-EGU points	0.96	Non-EGU points	0.96

Table 3. Evaluation of CAMx modeled NO_2 using OMI NO_2.

Inversion region	Priori			Posteriori: region-based inversion			Posteriori: sector-based inversion I			Posteriori: sector-based inversion II		
	R^2	NMB[b]	NME[c]	R^2	NMB	NME	R^2	NMB	NME	R^2	NMB	NME
HGB	0.57	-0.25	0.36	0.57	-0.17	0.35	0.57	-0.21	0.32	0.57	-0.18	0.34
DFW	0.74	-0.21	0.29	0.72	-0.21	0.28	0.70	-0.12	0.25	0.75	-0.13	0.30
BPA	0.40	-0.46	0.47	0.45	-0.33	0.43	0.37	-0.42	0.43	0.39	-0.43	0.44
NE Texas	0.24	-0.40	0.44	0.24	-0.36	0.43	0.21	-0.39	0.43	0.25	-0.31	0.42
Austin and San Antonio	0.45	-0.25	0.35	0.47	-0.18	0.35	0.43	-0.23	0.33	0.44	-0.23	0.34
Overall[a]	0.74	-0.11	0.17	0.75	-0.05	0.16	0.75	-0.04	0.14	0.75	-0.04	0.16

a. Compared to OMI observations in all inversion regions

b. Normalized mean bias: $\Sigma(\text{Mod-Obs})/\Sigma(\text{Obs})$

c. Normalized mean error: $\Sigma|(\text{Mod-Obs})|/\Sigma|(\text{Obs})|$

Table 4. Evaluation of CAMx modeled NO_2 using hourly AQS ground-measured NO_2.

Inversion region	Priori			Posteriori: region-based inversion			Posteriori: sector-based inversion I			Posteriori: sector-based inversion II		
	R^2	NMB	NME	R^2	NMB	NME	R^2	NMB	NME	R^2	NMB	NME
HGB	0.51	0.46	0.67	0.51	0.61	0.77	0.50	0.26	0.56	0.51	0.59	0.76
DFW	0.49	0.43	0.66	0.49	0.40	0.65	0.48	0.14	0.53	0.50	0.55	0.74
BPA	0.45	0.92	1.02	0.45	1.74	1.77	0.45	0.72	0.86	0.45	0.99	1.08
NE Texas	0.70	0.86	0.93	0.70	1.07	1.12	0.70	0.33	0.52	0.70	1.36	1.40
Austin and San Antonio	0.46	0.60	0.87	0.47	0.80	1.01	0.48	0.37	0.73	0.47	0.58	0.86
Overall[a]	0.51	0.51	0.72	0.48	0.67	0.85	0.50	0.26	0.59	0.51	0.63	0.81

a. Compared to all ground sites

Table 5. Evaluation of CAMx modeled NO_2 using P-3 aircraft-measured NO_2 and NO_y.

Statistical parameters	NO_2[a]				NO_y[a]			
	Priori	Posteriori: region-based inversion	Posteriori: sector-based inversion I	Posteriori: sector-based inversion II	Priori	Posteriori: region-based inversion	Posteriori: sector-based inversion I	Posteriori: sector-based inversion II
R^2	0.22	0.23	0.24	0.21	0.34	0.35	0.35	0.34
NMB	0.09	0.15	-0.02	0.17	0.70	0.76	0.54	0.79
NME	0.99	1.03	0.90	1.06	0.98	1.03	0.87	1.04

a. Comparison available for only four days (August 31, September 11, September 13, and September 15, 2006).

Table 6. Evaluation of CAMx modeled O_3 using hourly AQS ground-measured O_3.

Source region	Priori			Posteriori: region-based inversion			Posteriori: sector-based inversion I			Posteriori: sector-based inversion II			Sector-I inversed NO_x emissions & GOES photolysis		
	R^2	NMB	NME	R^2	NMB	NME	R^2	NMB	NME	R^2	NMB	NME	R^2	NMB	NME
HGB	0.46	0.68	0.75	0.47	0.67	0.74	0.46	0.65	0.72	0.45	0.70	0.76	0.54	0.62	0.69
DFW	0.64	0.21	0.32	0.64	0.23	0.33	0.64	0.18	0.29	0.64	0.21	0.33	0.66	0.18	0.28
BPA	0.47	0.66	0.70	0.47	0.59	0.66	0.49	0.60	0.64	0.45	0.69	0.73	0.52	0.59	0.63
NE Texas	0.49	0.36	0.43	0.49	0.38	0.44	0.50	0.32	0.40	0.48	0.37	0.45	0.55	0.30	0.38
Austin and San Antonio	0.52	0.40	0.46	0.52	0.40	0.46	0.52	0.35	0.43	0.52	0.42	0.48	0.57	0.34	0.41
Overall[a]	0.50	0.42	0.50	0.51	0.42	0.50	0.50	0.38	0.46	0.49	0.43	0.51	0.55	0.37	0.45

a. Compared to all ground sites

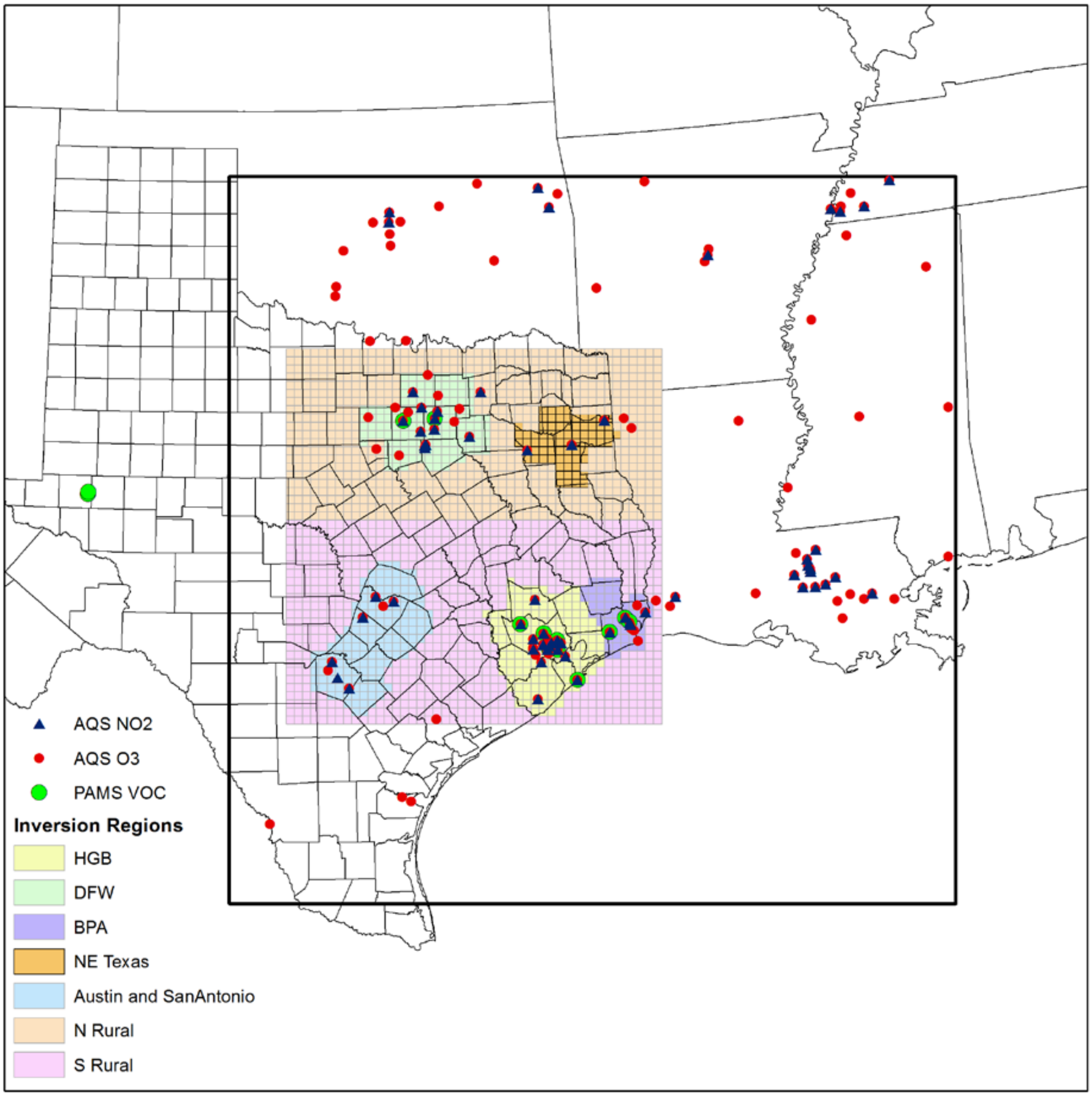

Figure 1. Seven designated inversion regions in eastern Texas (shaded) within 12-km CAMx modeling domain (black square) covered by ground NO_2 monitoring sites (blue triangles), VOC monitoring sites (green circles), and O_3 monitoring sites (red circles).

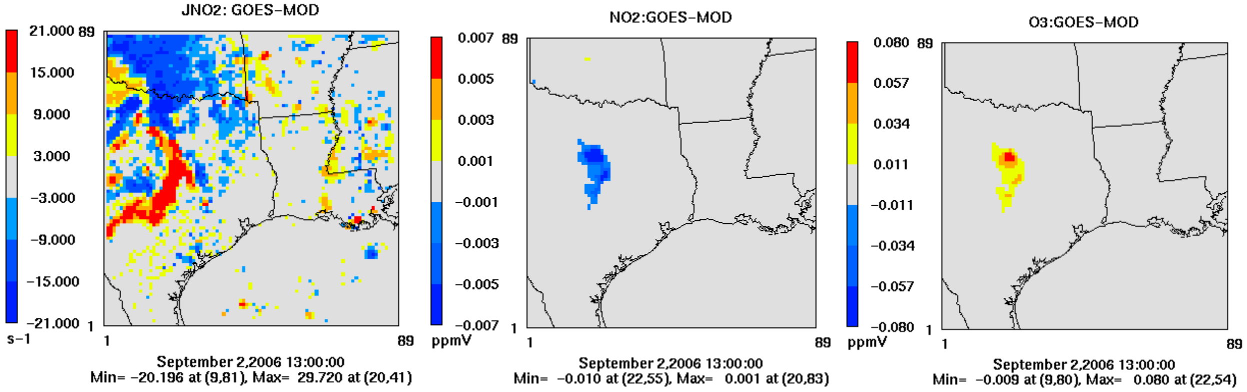

Figure 2. Differences between satellite-derived (GOES) and model predicted (MOD) J_{NO2} (left) in simulating NO_2 (middle) and O_3 (right) at 13:00 on 2 September 2006.

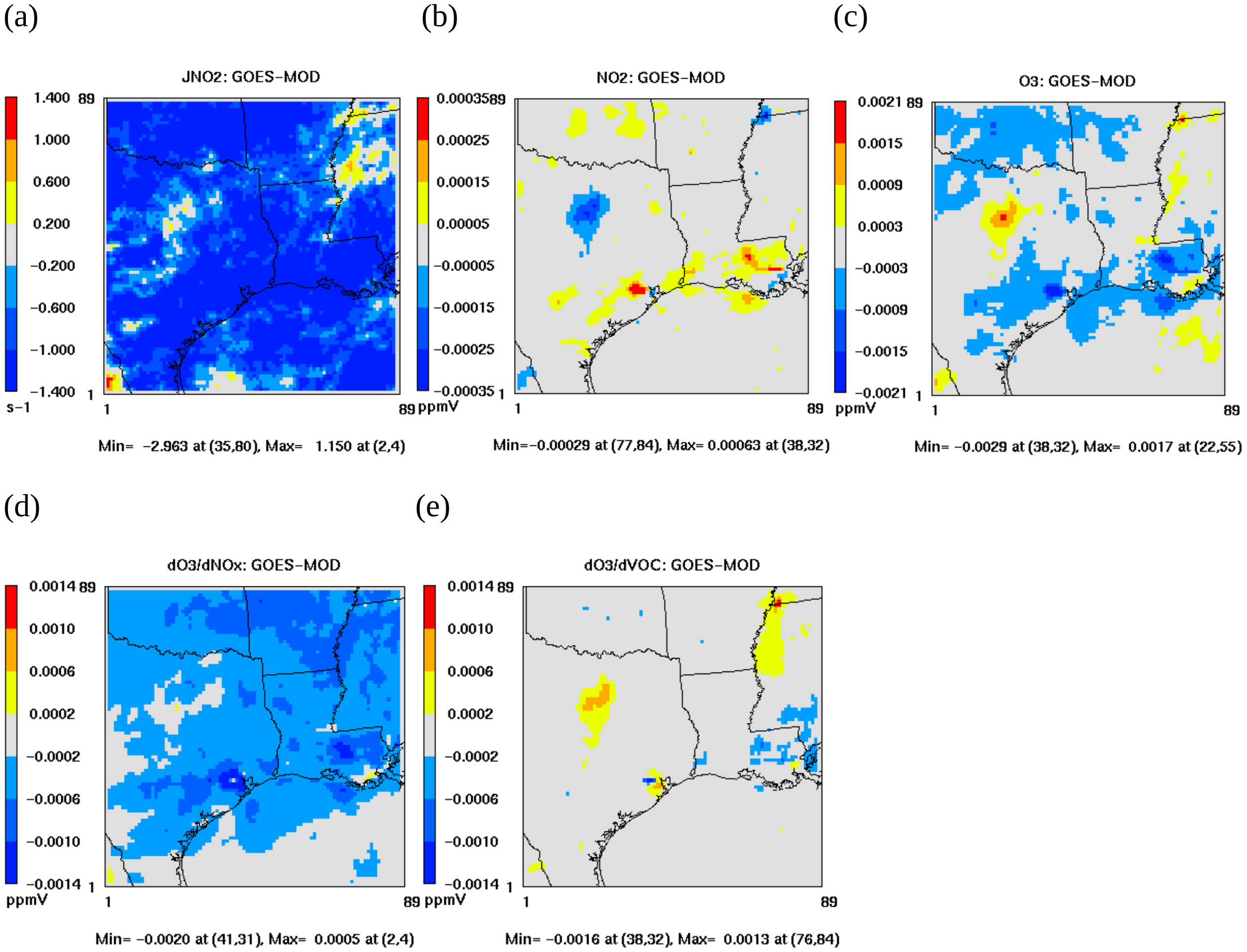
(a) (b) (c)

(d) (e)

Figure 3. Monthly 8-h (10:00-18:00LT) averaged differences between satellite-derived (GOES) and model predicted (MOD) (a) JNO_2 in simulating (b) NO_2, (c) O_3, and O_3 sensitivities to (d) NO_x and (e) VOC.

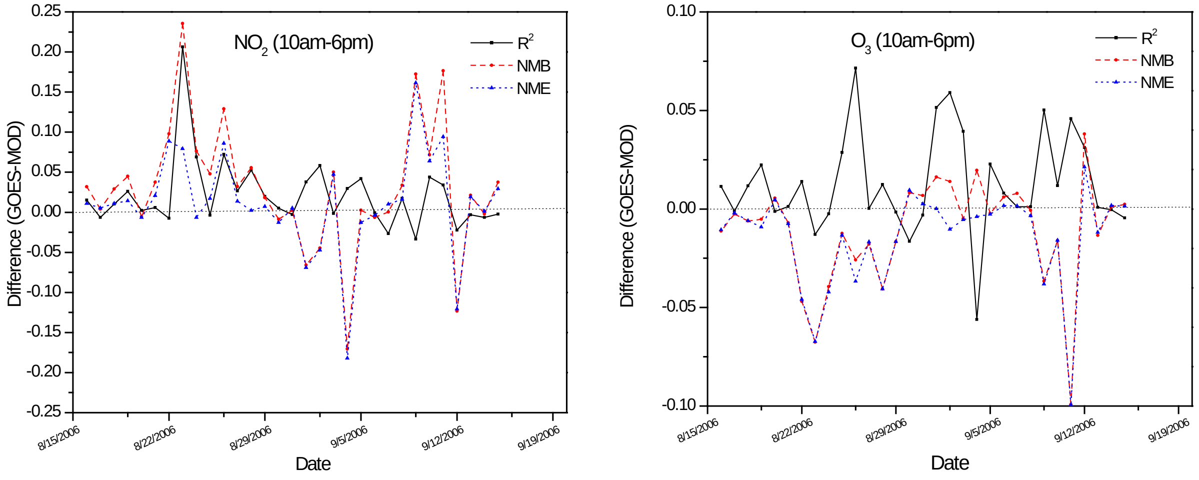

Figure 4. Change in model performance (R^2, NMB, and NME) in simulating daily 8 hours (10:00-18:00LT) NO_2 (left) and O_3 (right) caused by satellite-derived photolysis rates.

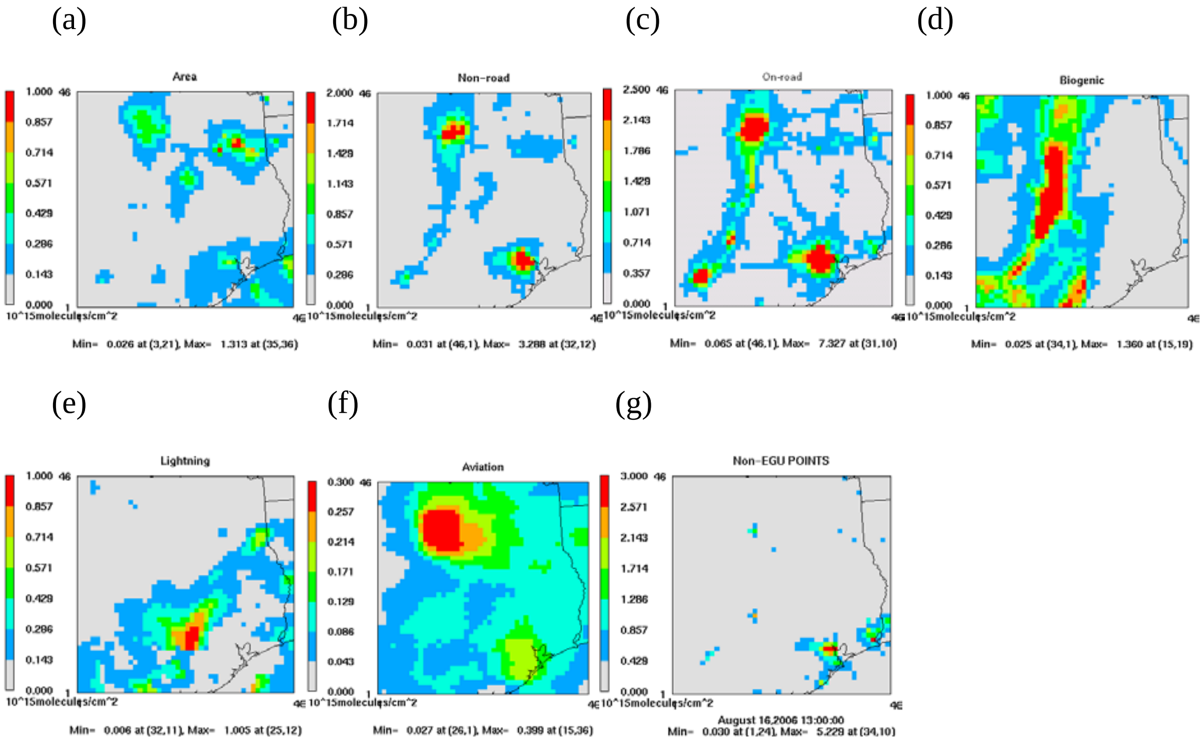

Figure 5. Vertical column densities of NO_2 sensitivities to NO_x emissions of (a) area, (b) non-road, (c) on-road, (d) biogenic, (e) lightning, (f) aviation, and (g) non-EGU points source sectors.

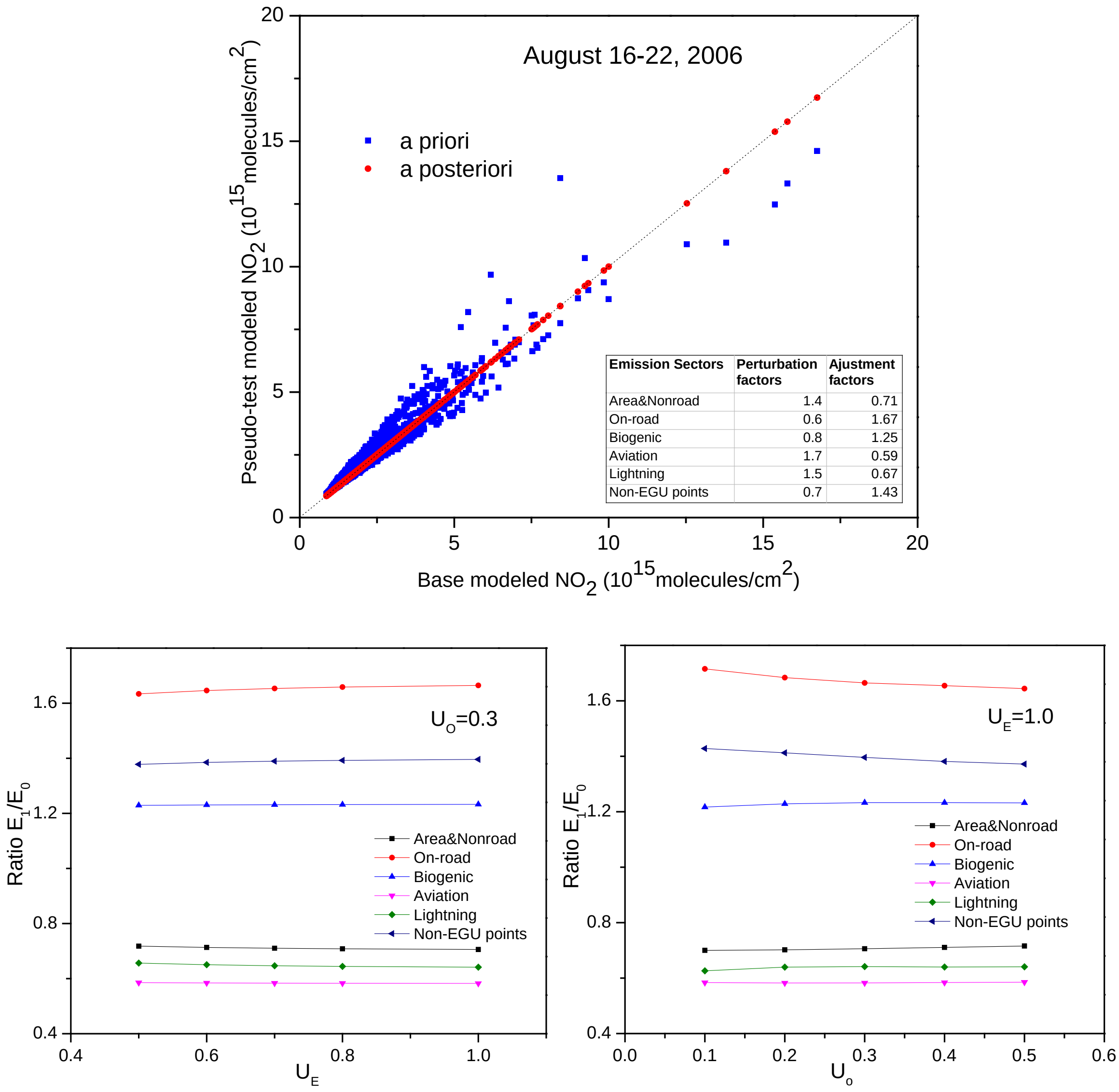

Emission Sectors	Perturbation factors	Ajustment factors
Area&Nonroad	1.4	0.71
On-road	0.6	1.67
Biogenic	0.8	1.25
Aviation	1.7	0.59
Lightning	1.5	0.67
Non-EGU points	0.7	1.43

Figure 6. Pseudodata analysis for the sector-based DKF inversion (top), and its sensitivities to varied uncertainties in emissions (U_E) (bottom left) with 30% uncertainty in observation (U_O) and in observations (bottom right) with 100% uncertainty in emissions.

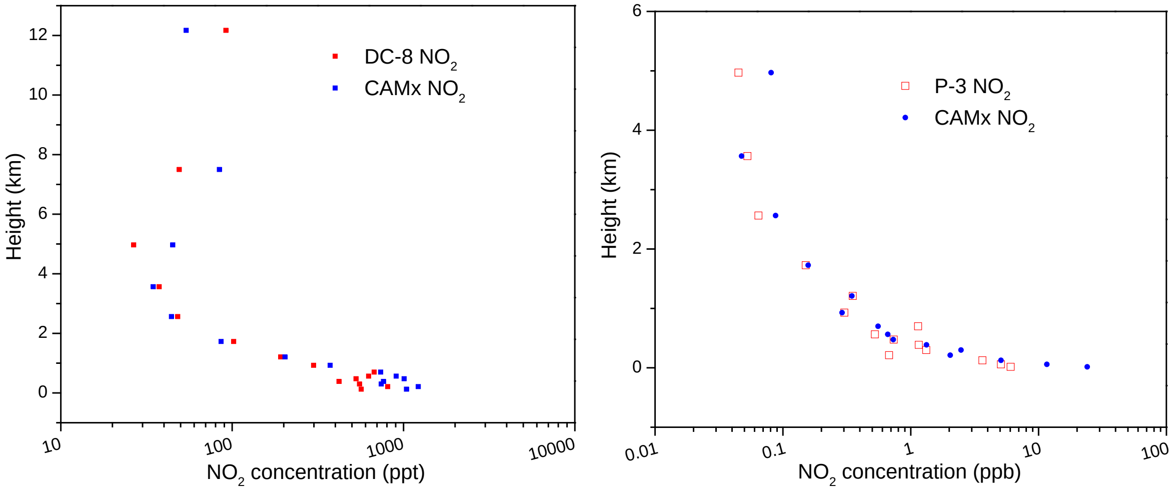

Figure 7. Comparisons of modeled NO_2 vertical distributions with INTEX NASA DC-8 flight (left) and TexAQS 2006 NOAA P-3 aircraft (right) measurements.

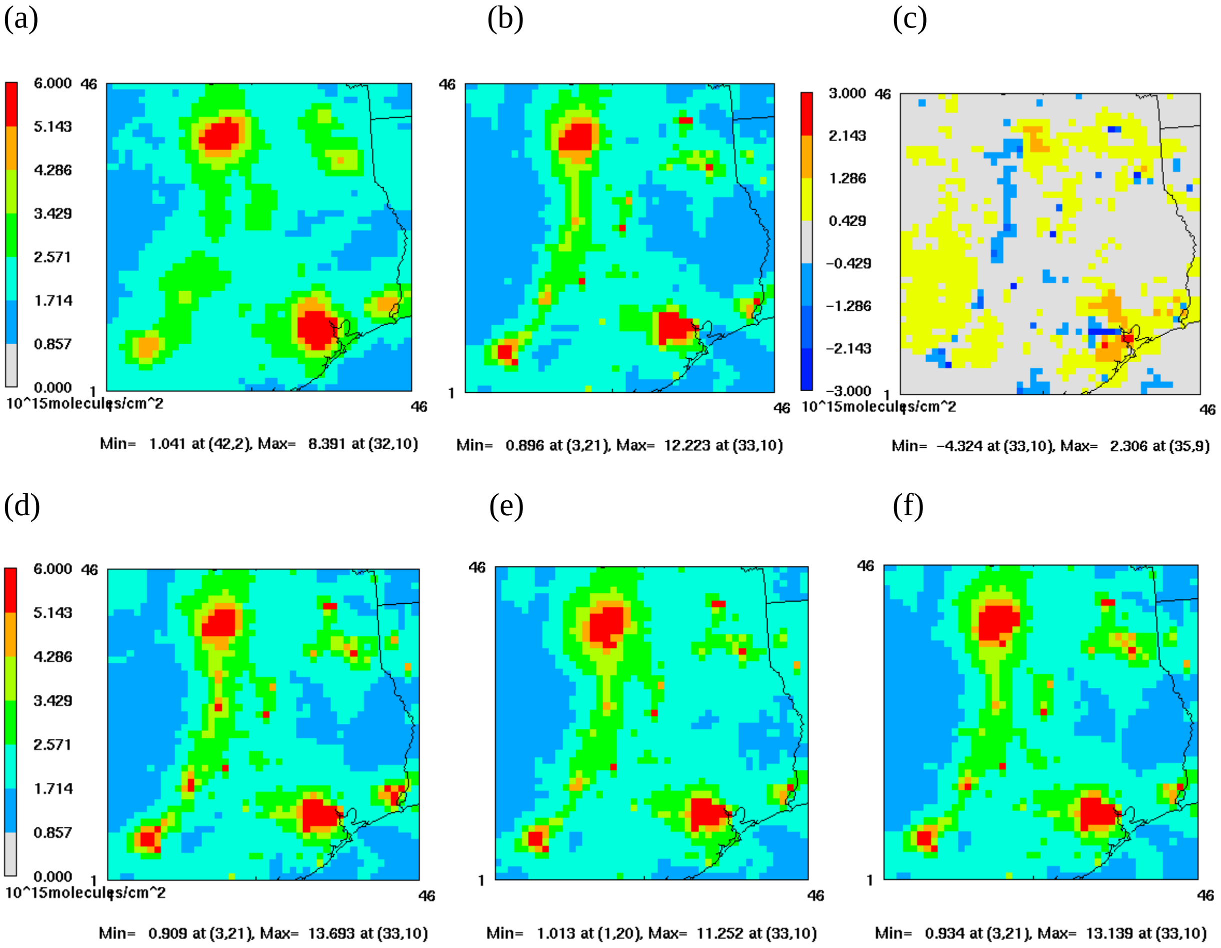

Figure 8. Monthly averaged (16 August to 15 September) tropospheric NO_2 VCDs at 13:00-14:00LT from (a) OMI, (b) a priori simulation, (c) difference between OMI and a priori simulation, and simulations using a posteriori NO_x emissions generated by (d) region-based DKF inversion, and sector-based DKF inversion (e) case I and (f) case II.

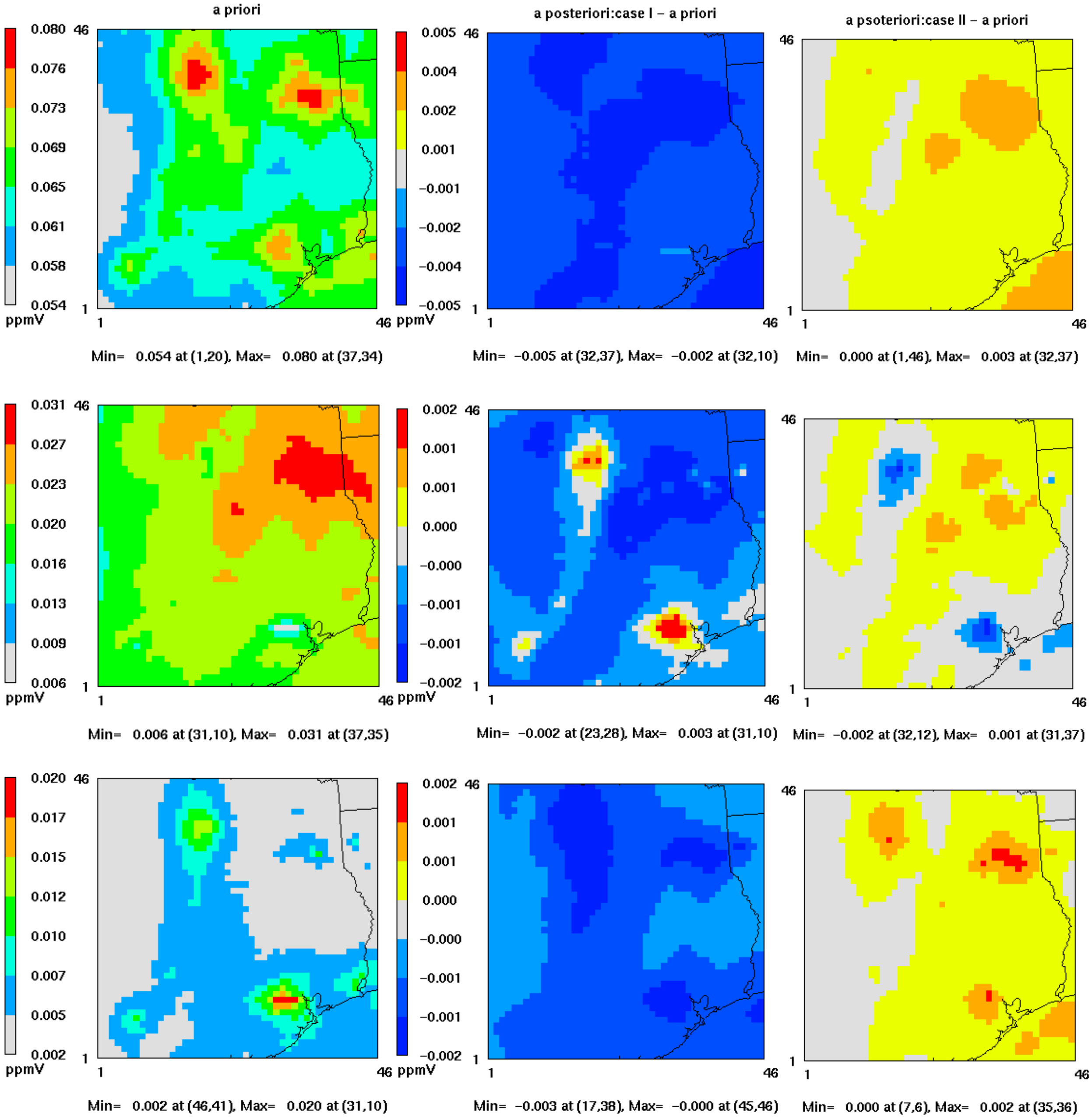

Figure 9. Monthly 8-h (10:00-18:00LT) averaged ground O_3 concentrations (top), O_3 sensitivity to NO_x (middle), and O_3 sensitivity to VOC (bottom) for the a priori case (left), and differences between a posteriori and a priori for the sector-based DKF inversions case I (middle) and case II (right).

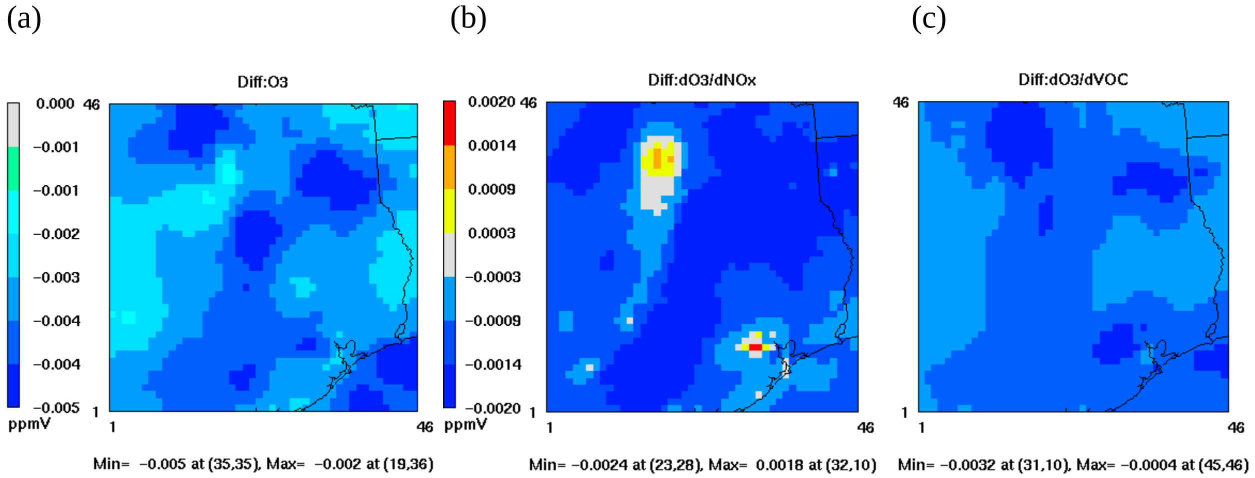

Figure 10. Monthly 8-h (10:00-18:00LT) averaged differences in modeled (a) ground O_3 concentrations, (b) O_3 sensitivity to NO_x, and (c) O_3 sensitivity to VOC resulting from use of both satellite-derived photolysis rates and NO_x emissions in place of a priori data.